Thermal behaviour and microstructure evolution of new ternary eutectic alloy in Al-Cu-Si-Ni system

Qing Cai, Changming Fang, Chamini Mendis, Isaac T.H. Chang *, Brian Cantor

Brunel Centre for Advanced Solidification Technology (BCAST), Brunel University London, Uxbridge, Middlesex UB8 3PH, UK

ARTICLE INFO

ABSTRACT

Eutectic alloys were fabricated from the quaternary Al-Cu-Si-Ni system via arc melting and suction casting. An invariant ternary eutectic reaction (α-Al+Si+θ-Al$_2$(CuNi)) was found in the quaternary alloy system with a composition of Al67.2Cu24Si8Ni0.8 (wt%). The dissolution of Ni ($\sim$1.7 at%) into tetragonal θ-Al$_2$Cu takes place during this ternary eutectic reaction. Density functional theory (DFT) calculations show that the configurational entropy stabilises this level of randomly substituted Ni with Cu sites in the θ-Al$_2$Cu lattice at high temperatures. The as-solidified eutectic microstructure exhibits a lamellar θ-Al$_2$(CuNi) phase showing fragmented lamellar morphology with a lamellar thickness of 130 $\pm$ 30 nm and Si exhibits fibrous morphology with a fibre diameter below 100 nm. The thermal stability of the Al-Cu-Si-Ni eutectic alloy after post-solidification annealing was investigated, and the thermal stability of the ternary eutectic microstructure is better than the corresponding Al33Cu (wt%) binary eutectic microstructure. It was found that Ni solution in θ-Al$_2$(CuNi) phase contributes to the thermal stability of this ternary eutectic microstructure and β_2-Al$_3$(CuNi)$_2$ (β_1-(Cu$_{2.9}$Ni$_{0.1}$)Al type, Fm-3 m) phase can transform from θ-Al$_2$(CuNi) phase after annealing at different temperatures. The Al-Cu-Si-Ni eutectic alloy has excellent as-cast hardness together with thermal stability. It is potentially valuable for the design of new aluminium alloys for serving at elevated temperatures.

1. Introduction

For decades, cast aluminium alloys have gained a lot of attention in the aerospace and automotive industry, due to their high specific strength (strength/density) and resistance to exposure at moderate temperatures [1–3] Cast aluminium alloys usually consist of a partial or complete eutectic structure, which plays an important role in their mechanical properties both at room and high temperatures [4,5]. In particular, Al-Cu based eutectic and hypoeutectic alloys have exceptional mechanical properties, due to a combination of precipitation [6–8] and Al-Cu eutectic strengthening [9–11]. A fine eutectic structure can be achieved via rapid solidification, leading to considerable improvement in strength [12]. In recent years, there has been large amount of research on the Al-Cu based multi-component eutectic or near-eutectic alloys. Adding more elements to the Al-Cu eutectic system can lead to a unique eutectic microstructure and thus improve physical or mechanical properties. For example, the bimodal eutectic structure was found in Al(13 at%)Cu (6 at%)Si ternary eutectic alloy, consisting of cellular binary eutectic (α-Al+Al$_2$Cu) and ternary eutectic matrix (α-Al+Al$_2$Cu+Si) [13,14]. This ternary eutectic alloy shows better toughness than binary Al-Cu eutectic alloy [15]. Moreover, Tiwary et al. studied the mechanical properties of ternary Al(10 at%)Cu(1.5 at%)Ni alloy [16]. The alloy consisting of primary Al$_7$Cu$_4$Ni (R-32 H) phase and binary eutectic matrix (α-Al+Al$_2$Cu), exhibits better mechanical properties than Al-Cu binary eutectic alloy at room and elevated temperature, resulting from the refined eutectic structure and primary Al$_7$Cu$_4$Ni (R-32 H) phase. In addition, similar Al-Cu based eutectic or near-eutectic alloys were also reported in ternary Al-Cu-Mg [17,18] and Al-Cu-Co [19] systems. Due to the complexity of the phase diagram and the lack of a suitable database, it is very difficult to predict the quaternary eutectic point. To date, only quaternary Al-Cu-Si-Mg [20] and Al-Cu-Si-Fe eutectic alloys [21] were reported. The four types of eutectic phases (α-Al, Si, Q-Al$_4$Cu$_2$Mg$_8$Si$_7$ and Al$_2$Cu) in Al-Cu-Si-Mg and (α-Al, Si, Al$_7$Cu$_2$Fe and Al$_2$Cu) in Al-Cu-Si-Fe were involved into these quaternary eutectic solidifications.

Furthermore, it is also known that Ni is very practical and effective for improving high-temperature mechanical performance. The addition of Ni into Al-Cu or Al-Si-Cu based piston alloys can lead to excellent mechanical properties at elevated temperatures ($\leq$350 °C), resulting from the formation of Ni-containing phases such as orthorhombic ε-Al$_3$Ni (Pnma), hexagonal Al$_3$Ni$_2$ (P-3m1),

---

rhombohedral Al_7Cu_4Ni (R-32 H), hexagonal Al_3CuNi (P-3m1) [16,22–24]. For instance, Zuo et al. investigated the effect of Ni in Al-Si-Cu cast piston alloy and found that the ultimate tensile strength at 250 °C increased from 162 MPa to 187 MPa with an increased volume fraction of ε-Al_3Ni from 1.03% to 8.2% [25]. The mechanical properties at elevated temperatures with the addition of Ni (0–1.5 wt%) in ternary Al-27 wt%Cu-5 wt%Si eutectic alloy were reported by Awe et al. [26]. The ultimate tensile strength at elevated temperature can be greatly improved as well as excellent elongation, with the addition of less than 1 wt%Ni. It can be concluded that Al-Cu-Si-Ni quaternary system has the potential for designing heat-resistant alloys.

The coarsening of microstructure in aluminium eutectic alloys can be usually found after their exposure to elevated temperatures, due to the driving force of reducing the interfacial energy of eutectic phases at high temperatures. Higher thermal stability of eutectic phases contributes to less sacrifice of the strength at high temperatures and it is favourable for the application of the alloys at elevated temperatures. A few investigations on the thermal stability of eutectic phases have been studied on different eutectic aluminium alloys, such as Al-Ni [27], Al-Ce [28,29], Al-Fe [30] and Al-Ni-Mn [31] systems. With respect to Al-Cu based alloys, most of the studies focused on preventing the coarsening θ'-Al_2Cu precipitates, and θ'-Al_2Cu is thermodynamically metastable over 250 °C [32–34]. However, the coarsening behaviour of eutectic phases is also important and they have a great impact on the mechanical performance of the alloys at elevated temperatures of cast alloys [35,36].

Motivated by the above concern, the eutectic point in the Al-Cu-Si-Ni system was explored and studied. Detailed microstructural characterisation of eutectic Al-Cu-Si-Ni alloy was performed to identify the phases. The hardness of studied Al-Cu-Si-Ni and Al-Cu binary alloys were compared. A post-solidification annealing was conducted in the eutectic Al-Cu-Ni-Si alloy to study the microstructure evolution of eutectic phases and their thermal stability. The dissolution of Ni into Al_2Cu was found in the system, leading to high hardness and thermal stability. It provides new insight into designing heat-resistant aluminium alloys in Al-Cu based system. The alloys based on Al-Cu-Si-Ni eutectic system are the potential for industrial applications at either room temperature or elevated temperature conditions.

2. Experimental

Small ~4 g ingots of various compositions were prepared by arc melting under an argon atmosphere with pure elements of Al (99.94%), Si (99.99%), Ni (99.98%), and Cu (99.99%). The ingots were arc melted and solidified with an Edmund Buhler arc melting system at least five times to ensure the homogeneity of the composition. Rod samples of 3 mm diameter and 30 mm length were prepared with suction casting into the water-cooled copper mould. The microstructure examination was taken from the middle part of the rod. The samples were cold mounted, ground and polished for characterisation with a Zeiss Supra 35 scanning electron microscope (SEM) equipped with energy-dispersive X-ray spectroscopy (EDX) operating at the voltage of 20 kV. The thickness of eutectic phases was analyzed by Image J software from SEM images. Bulk phase identification at room temperature and elevated temperatures was obtained in a Bruker D8 Advanced X-ray diffractometer (XRD) equipped with in situ heating chamber operating at 1×10^{-4} Pa, and using a Cu X-ray source and Ni filter at a voltage of 40 kV and a current of 40 mA with a step size of 0.24°/min. The 3D morphology of the eutectic was obtained via a focused ion beam and scanning electron microscopy technique, which is known as FIB-SEM tomography. The 3D structure was obtained from SEM slides using Dragonfly software, Version 2020.2 for Windows 10. Samples for transmission electron microscopy (TEM) were prepared by a Gatan

Precision Ion Polish system (PIPS) with voltage 2–5 kV and milling angles of 3.5–5°. The TEM samples were characterised with a JEOL 2100 F transmission electron microscope (TEM). The compositions of the phases were identified by EDX in JEOL 2100 TEM operated at 200 kV. The melting temperature and heat fusion were measured using a Netzsh 404F1 differential scanning calorimetry (DSC) with a heating/cooling rate of 5 K/min and dynamic flow of argon gas at a constant flow rate of 50 ml/min. The heat treatment was carried out in a Carbolite electric resistance furnace. For each heat treatment, the furnace was preheated to the designed temperature and held for 4 h, and after that, the samples were put inside, promptly. The samples were taken out and cooled in the air after each period. In the current work, the selected annealing temperatures are 350 °C and 500 °C. A temperature of 350 °C was selected because most of the heat-resistant aluminium alloys were used at the temperature below 350 °C, and the selection of 500 °C aims at the accelerating microstructure evolution during annealing. Vickers hardness measurements were performed with an FM-800 tester with a load of 5 kg and a dwell time of 15 s. An average hardness value was obtained from 8 measurements for each sample.

The Al33wt%Cu binary eutectic alloy was prepared to compare its properties with the newly developed alloy. It is named Alloy A. The composition of Al-Cu-Si-Ni eutectic alloy was obtained from the experimental method, as shown in Fig. 1. Firstly, a starting alloy with a composition of Al24Cu9Si1Ni (wt%) was prepared, which consisted of a mixture of binary cellular Al–Al_2Cu eutectic, Si/Ni-containing primary particles and a fine-scale ternary eutectic. The composition collected from the ternary eutectic microstructure region was measured by EDX analysis. Secondly, a new alloy with this measured ternary eutectic composition was prepared, which contained a much higher fraction of the fine ternary eutectic microstructure, but still with minor binary eutectic and primary α-Al and primary Si phase regions. The composition of the ternary eutectic was again measured in this secondary alloy by EDX. Thirdly, a new alloy with this newly measured ternary eutectic composition was prepared, which again contained a much higher fraction of the fine ternary eutectic structure. After this iterative procedure, the alloy consists almost completely of a very uniform ternary eutectic microstructure with only very minor residual regions of binary eutectic. In other words, the alloy composition was now very close to the true ternary eutectic composition in the Al-Cu-Si-Ni system. This final eutectic alloy with a composition of Al24Cu8Si0.8Ni (wt%) was named Alloy B. Apart from the eutectic alloy, the Al-Cu-Si-Ni alloys which have the composition around the eutectic point were prepared, aiming at investigating the solidification sequence. The names, compositions, microstructure and hardness of the Al-Cu-Si-Ni alloys are summarised in Table 1.

3. First-principles calculations

For a better understanding of the experimental observations, first-principles density functional theory (DFT) calculations for Ni-containing θ-Al_2Cu at ambient conditions were performed. Then, the related contribution of the configurational entropy to the stability of the Ni-doped θ-Al_2Cu crystals at elevated temperatures was estimated. A supercell approach for investigating Ni containing θ-Al_2Cu phase was employed. A $2a_0 \times 2a_0 \times 3c_0$ supercell, where a_0 and c_0 are the lattice parameters of θ-Al_2Cu unit cell was built [37]. In the Al-rich region of the ternary Al-Cu-Ni system, there are two stable phases, tetragonal θ-Al_2Cu and cementite-type ε-Al_3Ni [38]. These two binary compounds are used as references in the present theoretical study. The supercell used in the DFT calculations contained 48 chemical formula units.
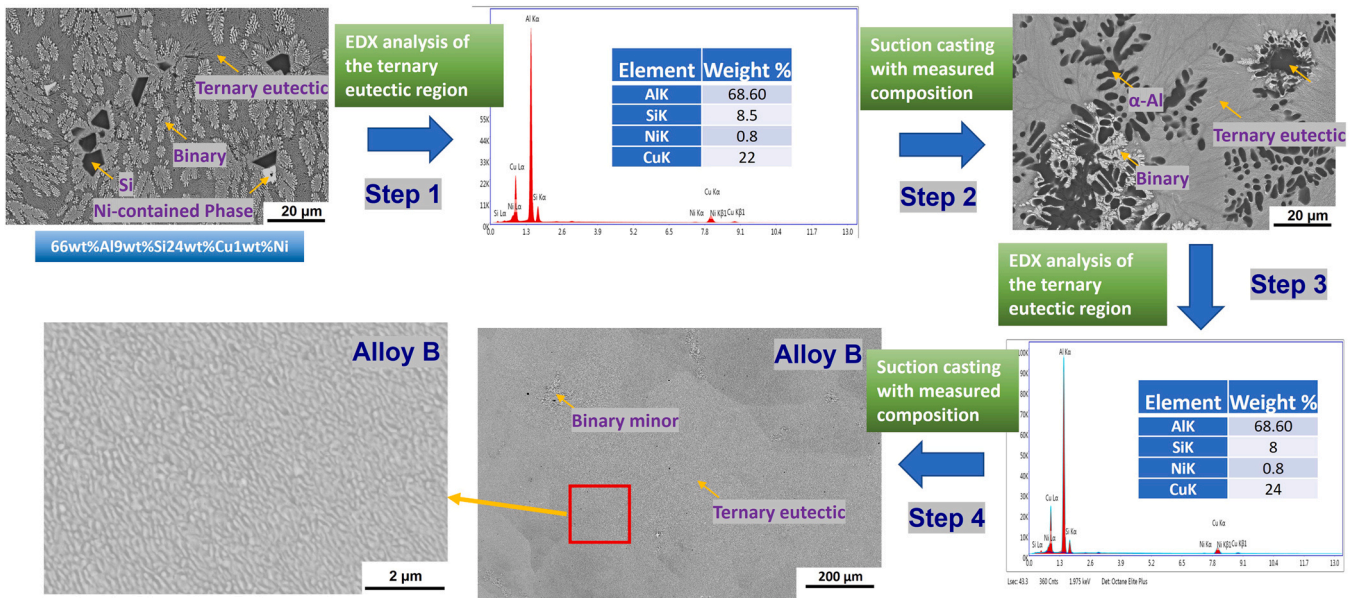
The Ni containing θ-Al_2Cu can be represented as:

Fig. 1. The illustration of steps for obtaining eutectic alloy composition in the Al-Cu-Si-Ni system.

$$(1-y/48)Al_{96}Cu_{48}+(x+y)Al_3Ni-(4x+y)Al=(Al_{96-x}Ni_x)(Cu_{48-y}Ni_y)+\Delta H \quad (1)$$

Here, ΔH is the reaction enthalpy. The formation energy ΔE for θ-$(Al_{96-x}Ni_x)(Cu_{46-y}Ni_y)$ is.

$$\Delta E = E[(Al_{96-x}Ni_x)(Cu_{48-y}Ni_y)]-\{(1-y/48)E[\theta-Al_{96}Cu_{48}]+(x+y)E(Al_3Ni)-(4x+y)E(Al)\} \quad (2)$$

Here, $E[\theta-(Al_{96-x}Ni_x)(Cu_{48-y}Ni_y)]$, $E[\theta-Al_{96}Cu_{48}]$, E(Al) and $E(Al_3Ni)$ are the calculated total valence-electron energies for θ-$(Al_{96-x}Ni_x)$ $(Cu_{48-y}Ni_y)$, θ-$Al_{96}Cu_{48}$, α-Al, θ-Al_2Cu and ε-Al_3Ni, respectively. The calculated formation energy, $\Delta E = -\Delta H$ at ambient conditions and zero-point vibration contribution is ignored.

The plane-wave approach which has been implanted in the code VASP (Vienna ab initio simulation package) for all the first-principles calculations is utilized [39]. The Gaussian smearing (smearing width being 0.1 eV) was employed. The projector augmented-wave (PAW) method within the generalized gradient approximation (PBE-GGA) is utilized [40,41]. Hubbard U correction was applied for the Cu 3d electrons [42]. The U=4 eV is adopted according to the literature [43,44]. For electronic structure calculations, we used cut-off energies of 520.0 eV for the wave functions and 700.0 eV for the augmentation functions. Dense k-meshes were used for sampling the electronic wave functions, e. g. a 12 × 12 × 16 (256 k-points) in the Brillouin zone (BZ) of θ-Al_2Cu in the Monkhost-Pack scheme [45].

4. Results

4.1. As-cast microstructures

The SEM backscattered images with the same magnification of the selected multi-component Al-Cu-Si-Ni alloys are displayed in Fig. 2(a-i). Alloy C has the highest content of Ni (1 wt%), and some polygon bright phases can be found in Fig. 2(a). These phases were identified as Ni-contained phases by SEM EDX (not shown here). With the decrease of Ni content in the alloy, there are almost no Ni-contained primary phases. The multi-component Al-Cu-Si-Ni alloys in the current study exhibit hierarchical morphology in the length scale of constituent phases. There are only three types of primary phases in these alloys, which are the Ni-contained phase, Si, and α-Al phases. Two types of eutectic structures with different length scales were observed. One type is binary cellular eutectic with Al_2Cu interlamellar spacing of 250–600 nm. Another type is a fine eutectic matrix with Al_2Cu interlamellar spacing of ~120 nm. The area fraction of the fine eutectic region can be increased by the modification of the compositions. The primary phases and types of eutectic structure in these alloys are summarised in Table 1.

Fig. 3(a) shows the XRD spectrum of the Al24Cu8Si0.8Ni (wt%) ternary eutectic alloy (Alloy B). There are only three eutectic phases in Alloy B which are Al_2Cu, Si and α-Al. The addition of Ni in the alloy does not lead to the formation of additional Ni-containing phases

Table 1
Chemical compositions, microstructures and hardness of the Al-Cu-Si-Ni alloys (wt%).

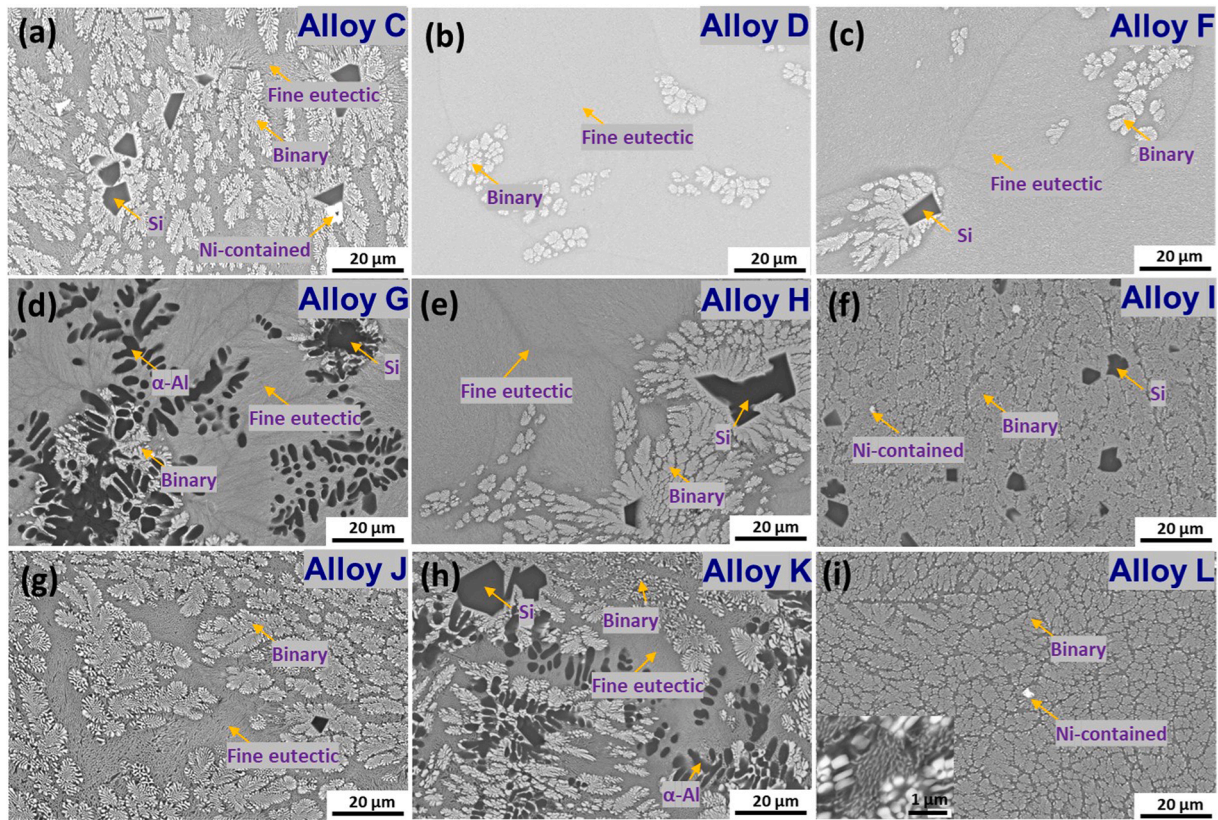| Alloy name	Composition (wt%)				Microstructure	Hardness (HV5)
	Al	Cu	Si	Ni		
Alloy A	67	33	-	-	$Al_2Cu+ \alpha$-Al (binary eutectic)	255 ± 6
Alloy B	67.2	24	8	0.8	$Al_2Cu+ \alpha$-Al+Si (ternary eutectic)	253 ± 6
Alloy C	66	24	9	1	β_2-phase+Si (primary), $Al_2Cu+ \alpha$-Al (binary eutectic), $Al_2Cu+ \alpha$-Al+Si (fine eutectic)	230 ± 13
Alloy D	67.7	24	7.5	0.8	$Al_2Cu+ \alpha$-Al (binary eutectic), $Al_2Cu+ \alpha$-Al+Si (fine eutectic)	248 ± 6
Alloy E	67.1	25	7	0.9	β_2-phase+Si (primary), $Al_2Cu+ \alpha$-Al (binary eutectic), $Al_2Cu+ \alpha$-Al+Si (fine eutectic)	231 ± 5
Alloy F	67.6	24	8	0.4	Si (primary), $Al_2Cu+ \alpha$-Al (binary eutectic), $Al_2Cu+ \alpha$-Al+Si (fine eutectic)	246 ± 5
Alloy G	68.7	22	8.5	0.8	α-Al+Si (primary), $Al_2Cu+ \alpha$-Al (binary eutectic), $Al_2Cu+ \alpha$-Al+Si (fine eutectic)	229 ± 11
Alloy H	65.2	25	9	0.8	Si (primary), $Al_2Cu+ \alpha$-Al (binary eutectic), $Al_2Cu+ \alpha$-Al+Si (fine eutectic)	248 ± 5
Alloy I	67.2	23	9	0.8	β_2-phase+Si (primary), $Al_2Cu+ \alpha$-Al (binary eutectic), $Al_2Cu+ \alpha$-Al+Si (fine eutectic)	210 ± 3
Alloy J	68.5	23.5	7.3	0.7	Si (primary), $Al_2Cu+ \alpha$-Al (binary eutectic), $Al_2Cu+ \alpha$-Al+Si (fine eutectic)	228 ± 8
Alloy K	68.7	21	9.5	0.8	α-Al+Si (primary), $Al_2Cu+ \alpha$-Al (binary eutectic), $Al_2Cu+ \alpha$-Al+Si (fine eutectic)	212 ± 4
Alloy L	67.1	26	6	0.9	β_2-phase(primary), $Al_2Cu+ \alpha$-Al (binary eutectic), $Al_2Cu+ \alpha$-Al+Si (fine eutectic)	237 ± 7

Fig. 2. SEM backscattered images of of-eutectic Al-Cu-Ni-Si alloys (a) Alloy C (b) Alloy D (c) Alloy F (d) Alloy G (e) Alloy H (f) Alloy I (g) Alloy J (h) Alloy K (i) Alloy L.

during the eutectic solidification. The microstructure of binary Al33wt%Cu alloy (Alloy A) is shown in Fig. 3(b) and (c). The two types of phases can be identified from the image. The bright phase is Al_2Cu, and the dark phase is α-Al. The microstructure has eutectic cells with two dominated phases, which are α-Al and Al_2Cu. The average interlamellar thickness of Al_2Cu in Alloy A is 100 ± 30 nm and it exhibits a regular structure. The SEM backscattered image in Fig. 3(d) shows the microstructure of the eutectic structure and the cell boundaries in Alloy B. The high-magnified image in Fig. 3(e) shows the Al_2Cu lamellae with an average thickness of 120 ± 30 nm, having fragment morphology. The size is very close to that of Alloy A. In addition, Vickers hardness was performed in these two eutectic alloys and off-eutectic Al-Cu-Si-Ni alloys. The hardnesses of Alloy A and Alloy B are 255 ± 6 HV_5 and 253 ± 6 HV_5 respectively, which are very close. They are higher than other off-eutectic alloys (Table 1).

DSC heating and cooling curves of Alloy B are displayed in Fig. 4(a). There is only one endothermic peak during heating corresponding to the ternary eutectic reaction, and the melting temperature is about 523 °C. However, there are mainly three peaks on the exothermic peak during cooling from the melt. The microstructure of Alloy B after DSC is shown in Fig. 4(b). The microstructure consists of primary α-Al, binary coarse eutectic and fine ternary eutectic. The pre-peaks in the exothermic peak in Fig. 4(a) correspond to the initial solidification of small amounts of primary α-Al and binary α-Al+Al_2Cu eutectic, followed by the main peak corresponding to the solidification of ternary α-Al+Al_2Cu+Si eutectic. The SEM EDX mapping of the fine eutectic region from Fig. 4(b) is shown in Fig. S1 (Supplementary Material). It is revealed that there are three types of eutectic phases (α-Al, Al_2Cu and Si) and the dissolution of Ni in Al_2Cu phase is found.

TEM bright-field images and corresponding selected area diffraction patterns (SADPs) in Fig. 5(a) reveal that the fine-scale features result from the ternary eutectic reaction in Alloy B. There are

three phases in the microstructure which are α-Al, Al_2Cu and Si as identified from corresponding SADPs. The Al_2Cu shows a fragmented lamellar morphology with a size below 200 nm. The distribution of the α-Al, Si, and Al_2Cu eutectic phases are also shown in the HAADF-STEM image from Fig. 5(b). Small (< 100 nm) Si particles are attached to the Al_2Cu fragment lamellae. EDX analysis under TEM was performed in a few Al_2Cu phases in Alloy B, shown in Fig. 5(c). The average composition of the Al_2Cu phase is $Al_{69.4}Cu_{28.9}Ni_{1.7}$ (at%). The normal lattice parameter of Al_2Cu is a=b= 6.06 Å and c= 4.87 Å [37]. However, the lattice parameter of Al_2Cu in the ternary eutectic alloy measured from SADP is a=b= 5.82 Å and c= 4.79 Å, which is smaller than the standard lattice parameter of Al_2Cu phase. Thus, the smaller lattice parameter is caused by the dissolution of Ni into the Al_2Cu phase. Interestingly, the dissolution of Ni in Al_2Cu was also found in Alloy B at slow solidification conditions (after DSC measurement at 5 K/min), shown in Fig. S1 (Supplementary Material).

Fig. 6 shows the 3D reconstruction of fine ternary eutectic in Alloy B. The morphology of Al_2Cu phase in Alloy B exhibits a less regular and fragmented lamellar morphology, which is different from that in binary Al-Cu eutectic alloys. The fragment of the lamellar indicates the instability of the lamellar growth. The Si phase has shot fibre morphology aligned together with the lamellar Al_2Cu phase, showing the cooperative growth of the eutectic phases. The lamellar morphology (Al_2Cu) and fibre morphology (Si) correspond well with the volume fraction of the eutectic phases [46].

4.2. Microstructure evolution after annealing

In order to study the thermal stability, Alloy B was annealed at different temperatures for different times. Fig. 7(a-c) and (d-f) show the backscattered images of Alloy A and Alloy B after annealing, respectively. The as-cast lamellar thickness of Al_2Cu in Alloy A is 100 ± 30 nm as shown in Fig. 3(b), and it coarsens to ~4 μm after
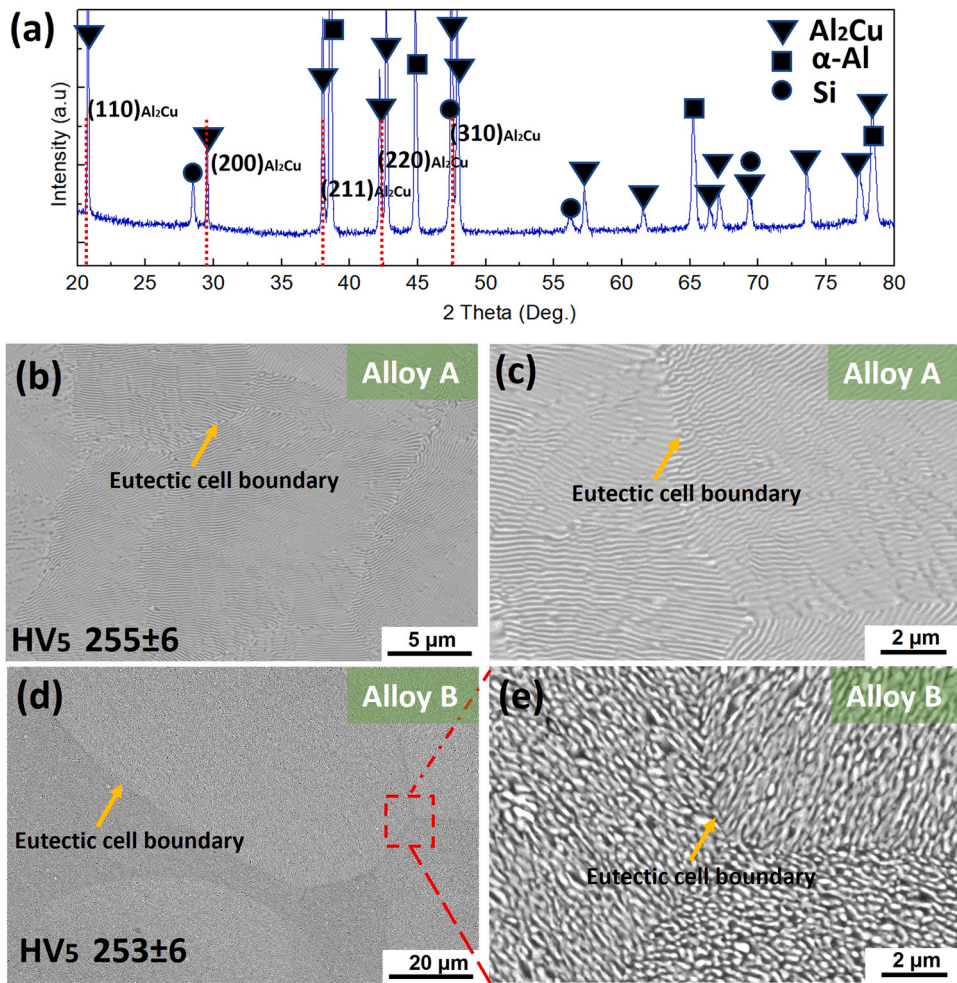
Fig. 3. (a) The XRD spectrum of Alloy B (b) SEM backscattered images showing the microstructure of Alloy A under low magnification (c) the eutectic cell boundary of Alloy A under high magnification; (d) SEM backscattered images showing the microstructure of Alloy B under low magnification (e) the eutectic cell boundary under high magnification from (d).

168 h annealing at 350 °C shown in Fig. 7(a). In comparison, the as-cast lamellar thickness of Al_2Cu phase in Alloy B changes from ~130 nm to ~1.5 µm after the same condition shown in Fig. 7(d). A similar phenomenon of a slower coarsening rate is also present in Fig. 7(b,e) and (c,f). It is revealed that the microstructure of Alloy B has much better thermal stability.

In addition, the high-magnified SEM-backscattered images of microstructures in Alloy B after annealing for various temperatures and times, are present in Fig. 8(a-d). It can be found that there are some fine brighter phases attached to the Al_2Cu phases, which are marked by red dash circles. It is indicated that there are some new phases formed in Alloy B after annealing at different temperatures.
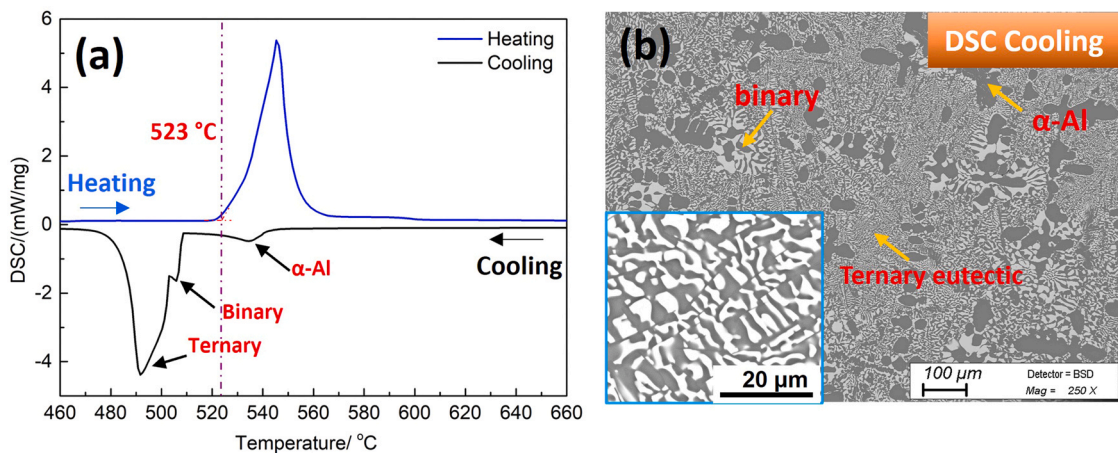

Fig. 4. (a) DSC heating and cooling curves of Alloy B (b) SEM backscattered image showing the microstructure after DSC measurement with an inserted high-magnified image of the ternary eutectic region.
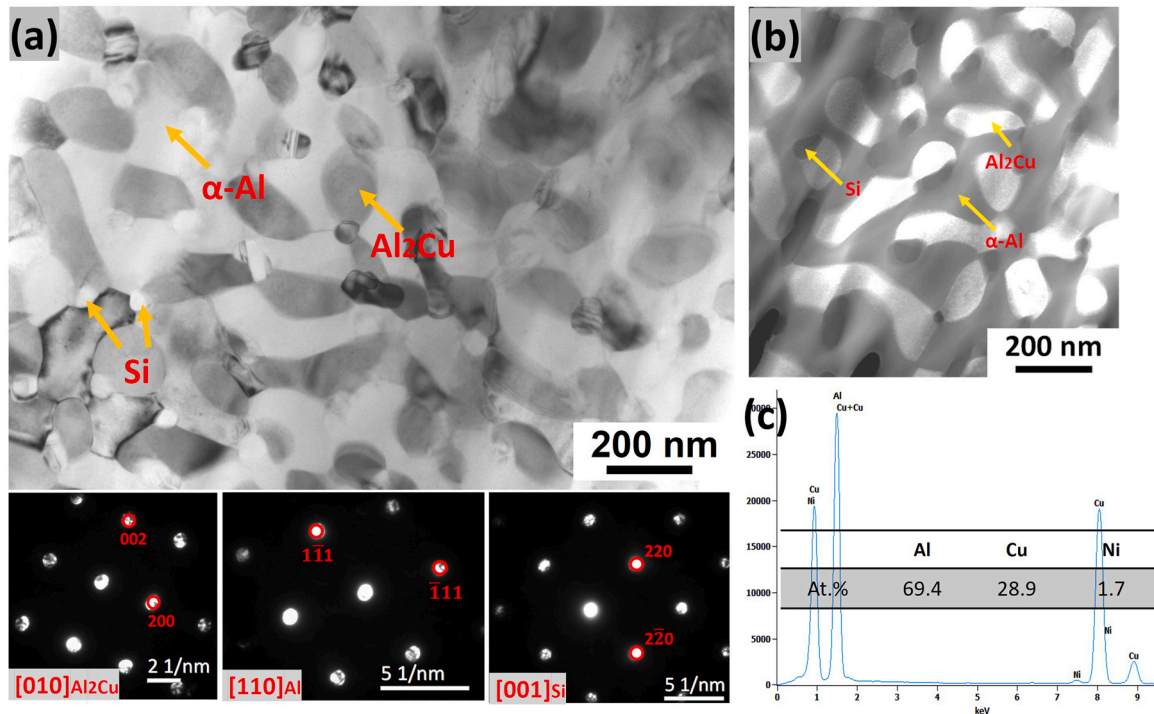
Fig. 5. (a) TEM bright-field image of Alloy B with corresponding SADPs (b) HAADF-STEM image (c) EDX analysis of Al$_2$Cu phase.
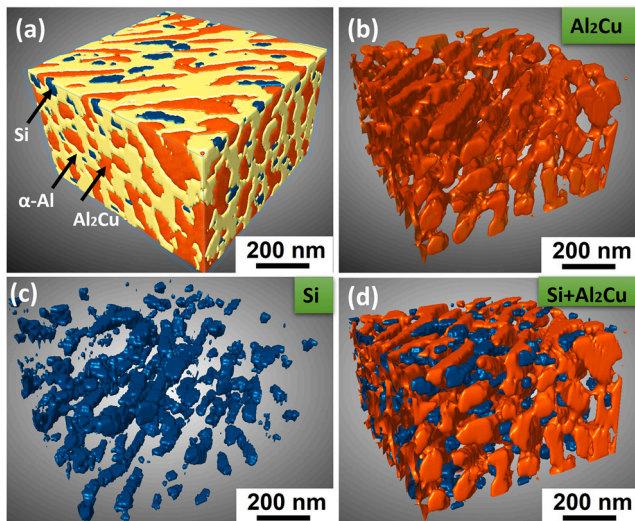

Fig. 6. The morphology of eutectic phases in Alloy B obtained from FIB-SEM tomography technique (a) three eutectic phases of α-Al, Si and Al$_2$Cu (b) Al$_2$Cu phase (c) Si phase (d) Al$_2$Cu and Si phases.

The dual-size distribution of the bright intermetallic phase was found in Fig. 8(c) and (d). Under as-cast conditions, Al$_2$Cu phase in Alloy B dissolves ∼1.7 at% of Ni and it can be induced that these brighter phases are Ni-contained phases which developed from Al$_2$Cu phase. It is further confirmed that the better thermal stability of Al$_2$Cu phase in Alloy B results from the dissolution of Ni.

Fig. 9(a) shows TEM bright-field image with inserted HAADF-STEM image of the microstructure of Alloy B after annealing for 168 h at 350 °C, corresponding to the SEM results in Fig. 8(a). EDX mapping of this region is shown in Fig. 9(b), and the Ni-rich region indicates the phase transformation. The composition of this phase is about 62Al33.1Cu4.9Ni (at%) from the EDX point analysis under TEM, shown in Table 2. Three SADPs were obtained from the Ni-

containing phase under different zone axis after annealing shown in Fig. 9(c), and it was identified to be β$_1$-(Cu$_{2.9}$Ni$_{0.1}$)Al-type phase [47]. β$_1$-(Cu$_{2.9}$Ni$_{0.1}$)Al phase has FCC crystal structure and the lattice parameter is a=b=c= 5.841 Å and α = β = γ = 90°. Here, the Ni-containing phase is named β$_2$ phase. The structural formula of β$_2$ phase is close to Al$_3$(CuNi)$_2$.

Fig. 10 (a) shows the TEM bright-field image with inserted HAADF-STEM image of the microstructure of Alloy B after annealing at 500 °C for 5 h. β$_2$ phase (β$_1$-(Cu$_{2.9}$Ni$_{0.1}$)Al-type) was also identified from the SAPDs in Fig. 10 (c). The crystal structure and lattice parameter of the formed β$_2$ phase after annealing at 500 °C for 5 h are almost the same as that after annealing at 350 °C for 168 h, shown in Table 2. However, the composition of β$_2$ phase is about 61.8%Al31.2%Cu7.0%Ni (at%), which is different from that after annealing at 350 °C for 168 h, as shown in Table 2. However, based on the composition in Table 2, β$_2$ phase was also found with a structural formula of Al$_3$(CuNi)$_2$ [48]. The ratio of Cu:Ni in β$_2$ phase which formed at 500 °C is lower than that at 350 °C. The EDX mapping of the region is displayed in Fig. 10 (b). It is clearly shown that β$_2$ phase developed from Al$_2$Cu phase indicated by the high Ni element. Al$_2$Cu phase contains the minor Ni element. Si phase shows fibrous morphology with a diameter below 1 μm, and some Si phases are entrapped inside Al$_2$Cu phase with a smaller size of ∼500 nm.

Fig. 11 (a) shows HRTEM and the FFT images of the interface between Al$_2$Cu and β$_2$-phases in Alloy B annealed at 500 °C for 5 h. The schematic of the FFT diffraction pattern is displayed in Fig. 11 (b). The orientation relationship was found to be $(2\bar{2}0)_{β2}$ // $(2\bar{2}0)_{Al2Cu}$ and $[111]_{β2}$ // $[111]_{Al2Cu}$. The lattice disregistries of β$_2$/Al$_2$Cu can be calculated by the method proposed by Nabarro [49] as $F_{β2/Al2Cu}$ = $2(nd_{β2}- md_{Al2Cu})/ (nd_{β2}+md_{Al2Cu})$. Where $F_{β2/Al2Cu}$ is the disregistres, $d_{β2}$ and d_{Al2Cu} are corresponding D-spacings, n and m are integers. The D-spacing of $(2\bar{2}0)_{β2}$ and $(2\bar{2}0)_{Al2Cu}$ measured from SADPs are 0.210 nm and 0.215 nm, respectively. Here, m and n can be taken as 1. The calculated $F_{β2/Al2Cu}$ is −2.35%. This indicated the interfacial structure is semi-coherent and has low strain energy, which encourages the nucleation of the β$_2$ phase.
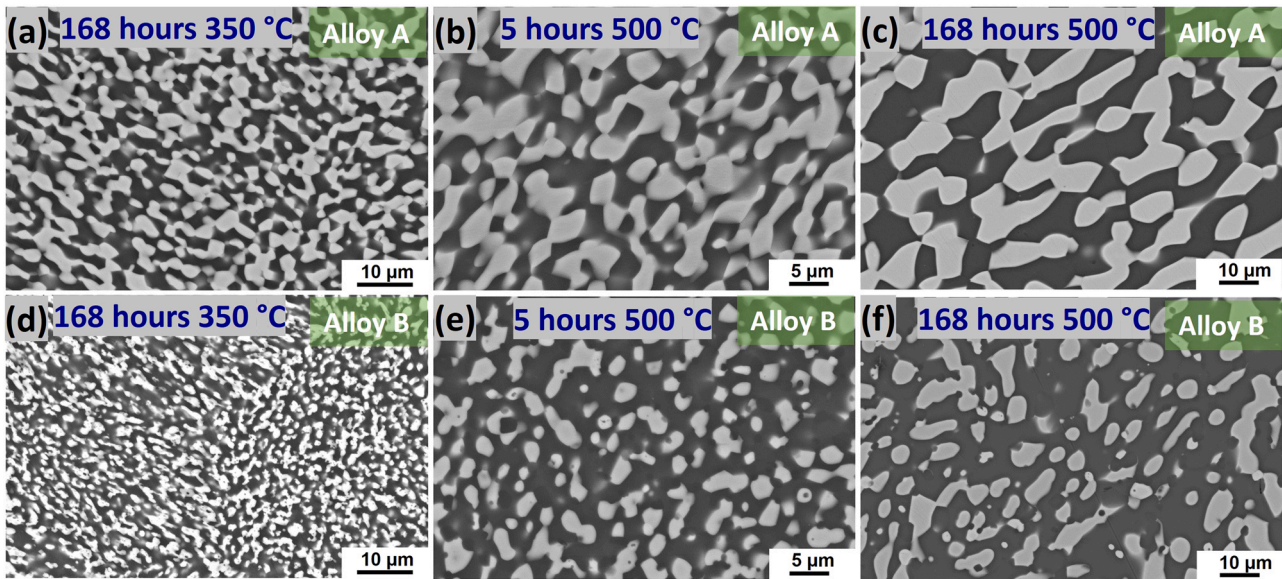
Fig. 7. SEM backscattered images showing the microstructure after annealing for different times and temperatures (a) Alloy A and (d) Alloy B annealed for 168 h at 350 °C; (b) Alloy A and (e) Alloy B annealed for 5 h at 500 °C; (c) Alloy A and (f) Alloy B annealed for 168 h at 500 °C.
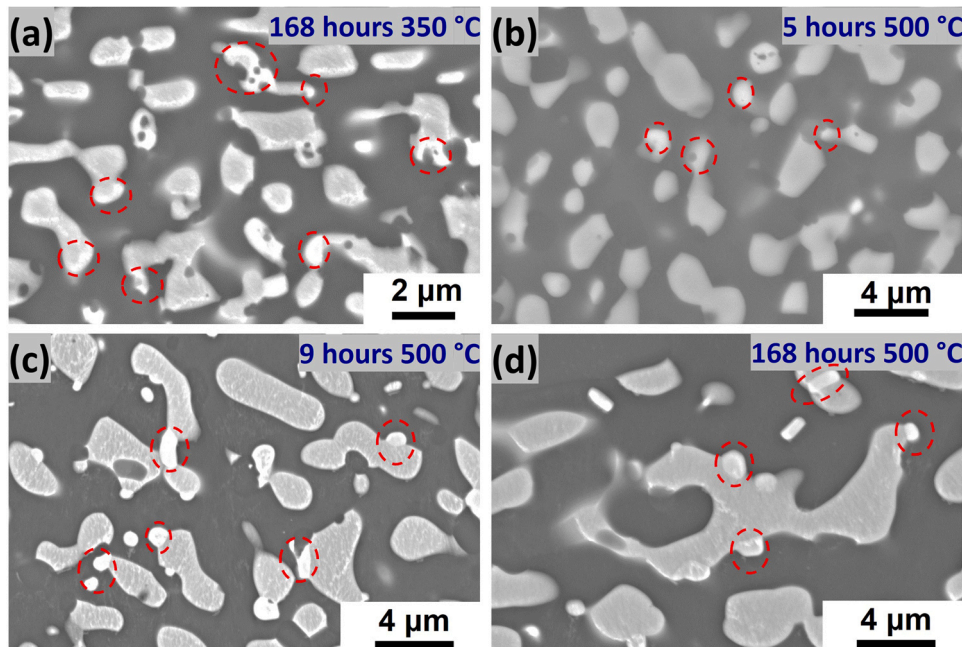

Fig. 8. enlarged images showing the phase transformation in Alloy B (a) 168 h at 350 °C (b) 5 h at 500 °C (c) 9 h at 500 °C (d) 168 h at 500 °C.

The average phase composition and lattice parameters of Al_2Cu and β_2 phase in Alloy B under as-cast and after annealing at different times and temperature are summarised in Table 2. The average compositions and lattice parameters of β_2 and Al_2Cu phase were obtained from TEM EDX and SAPDs, respectively. The lattice parameters of a and b in Al_2Cu increase as the Ni content in Al_2Cu decrease from 1.7% to 0.6% (at%) after 5 h of annealing, and there is almost no change in Ni content in the Al_2Cu phase with further annealing at 500 °C. The composition of β_2 phase is closer to the structural formula of $Al_3(CuNi)_2$ after annealing at 500 °C for different times. In addition, the lattice parameters of β_2 phase are very close in Alloy B annealed for different times at 500 °C and 350 °C, which indicates the phase transformation takes place via the diffusion of elements at different temperatures without changing its crystal structure.

5. Discussion

5.1. As-cast microstructure and hardness of Al-Cu-Si-Ni ternary eutectic alloy

It is reported that there is a quaternary eutectic reaction in the equilibrium Al-Cu-Si-Ni system, which is L→α-Al+ θ-Al_2Cu+Si+ γ-Al_7Cu_4Ni at ~520 °C [38,50]. γ-Al_7Cu_4Ni (Al_3Ni_2 type, hR12, R32H) has a rhombohedral-distorted B2 lattice (hexagonal) [51–53]. The lattice parameters are a=b= 4.105 Å and c= 39.9 Å. However, in the current study, the Al-based eutectic (Alloy B) was fabricated and a ternary eutectic reaction (α-Al+θ-$Al_2(CuNi)$+Si) occurred in this quaternary Al-Cu-Si-Ni system. For simplification, θ-$Al_2(CuNi)$ is named Al_2Cu phase. The Ni is involved in the ternary eutectic reaction with its dissolution into Al_2Cu phase under either rapid or
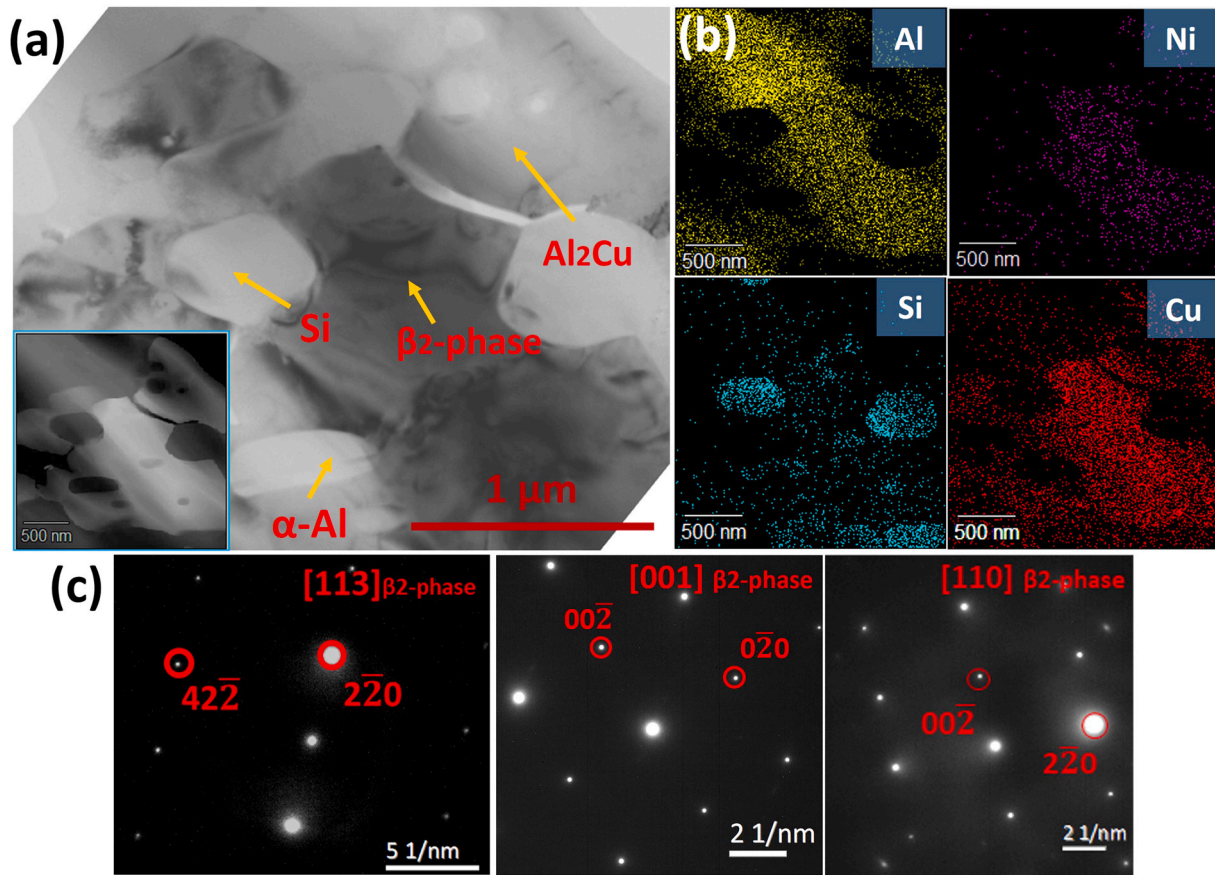
Fig. 9. (a) TEM bright-field image of Alloy B with inserted HAADF-STEM image showing the phase transformation after annealing for 168 h at 350 °C (b) the EDX mapping of phase transformation region (c) the corresponding SADPs of β_2-phase.

slow cooling rates and Alloy B shows a very uniform fine eutectic structure. It is different from the microstructure in so-called bimodal Al-Cu-Si [54] or Al-Si-Mg ternary eutectic alloys [55,56], having binary cellular eutectic and ternary eutectic matrix. In addition, ternary eutectic reactions have not been found in the ternary Al-Cu-Ni alloys [16,57]. Instead, the fine eutectic matrix in these Al-Cu-Ni alloys is lamellar Al-Al$_2$Cu binary eutectic. Overall, there is a lack of thermodynamic information on the quaternary Al-Cu-Si-Ni system, and more work needs to be done for the completion of the phase diagram.

Furthermore, it is known that ternary eutectic solidification is a diffusion-controlled process with a short diffusion layer along a solid-liquid front [58,59]. During the solidification in Alloy B, the transversal diffusion along solid/liquid interface is very complex. Al$_2$Cu phase absorbs Al, Cu and Ni elements while rejecting Si. α-Al

and Si also absorb Al and Si respectively as well as rejecting excessive elements. During rapid solidification, the short transversal diffusion is favourable for the development of the eutectic structure at high growth rates, resulting in fine interlamellar/rod spacing. The interlamellar spacing in binary eutectic alloys is linear to the undercooling in the solid/liquid front, based on Jackson and Hunt model [46,60]. This also shows a similar trend in ternary eutectic alloys [61,62]. Thus, the additional elements can provide high constitutional undercooling, which results in finer interlamellar spacing. In a multicomponent quaternary alloy, solidification tends to be initiated with a primary phase, then a binary eutectic and then a multicomponent eutectic as the liquid is enriched in alloying elements by the rejection of solute at the solid/liquid interface. The lamellar structure arises from a balance between minimising the total interfacial energy (promoted by a large spacing) and

Table 2
The compositions of Al$_2$Cu phase and β_2 phase as well as their lattice parameters under as-cast and after annealing in Alloy B.

| Alloy temper	Al$_2$Cu phase				β_2-phase (β_1- (Cu$_{2.9}$Ni$_{0.1}$)Al type)			
	Composition (at%)			Lattice parameter (Å)	Composition (at%)			Lattice parameter (Å)
	Al	Cu	Ni		Al	Cu	Ni	
As-cast	69.4	28.9	1.7	a=b= 5.82; c= 4.79	–	–	–	–
Annealing (500 °C for 5 h)	69	30.2	0.6	a=b= 5.94; c= 4.80	61.8	31.2	7.0	a=b=c= 5.90
Annealing (500 °C for 9 h)	69.6	29.9	0.5	a=b= 5.97; c= 4.81	61.2	31.6	7.2	a=b=c= 5.88
Annealing (500 °C for 168 h)	68.6	30.9	0.5	a=b= 5.96; c= 4.80	59.9	32.8	7.3	a=b=c= 5.82
Annealing (350 °C for 168 h)	68	31.6	0.4	a=b= 5.95; c= 4.82	62	33.1	4.9	a=b=c= 5.87
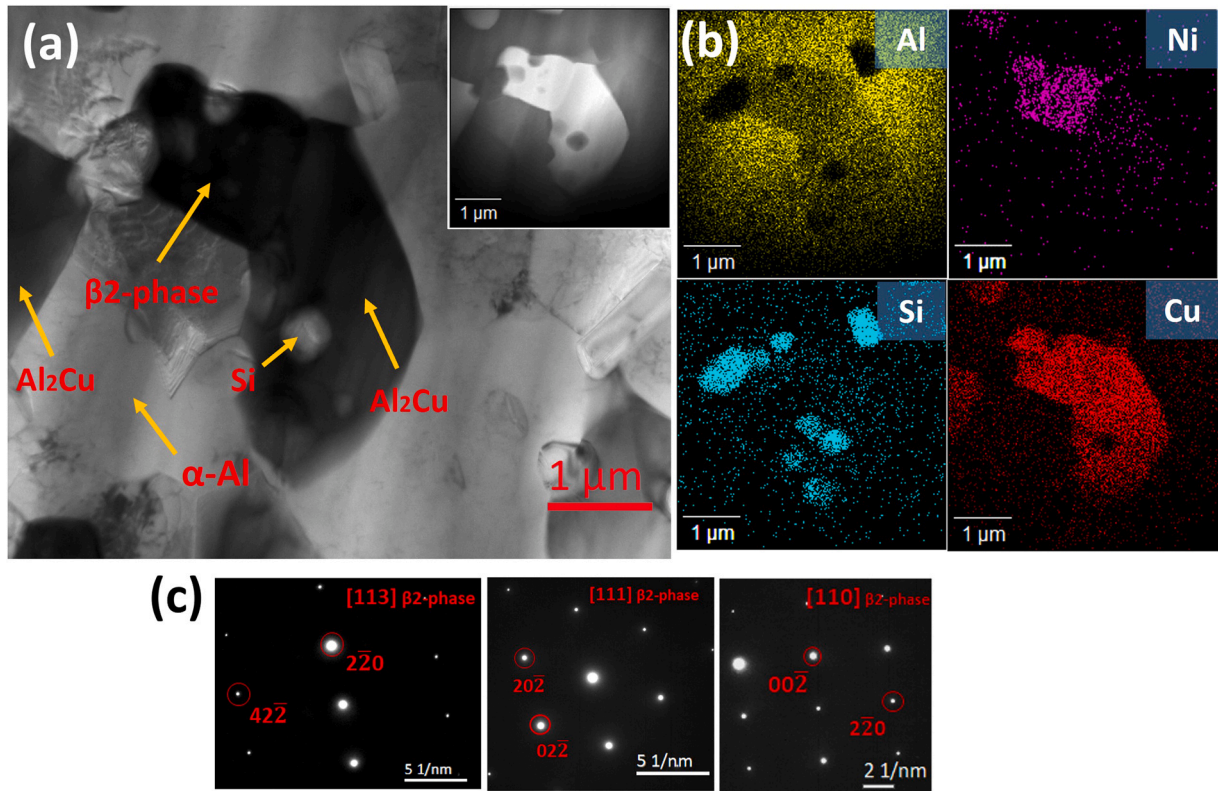
Fig. 10. (a) TEM bright-field image of Alloy B with inserted HAADF-STEM image showing the phase transformation after annealing for 5 h at 500 °C (b) the EDX mapping of phase transformation region (c) the corresponding SADPs of β_2-phase.
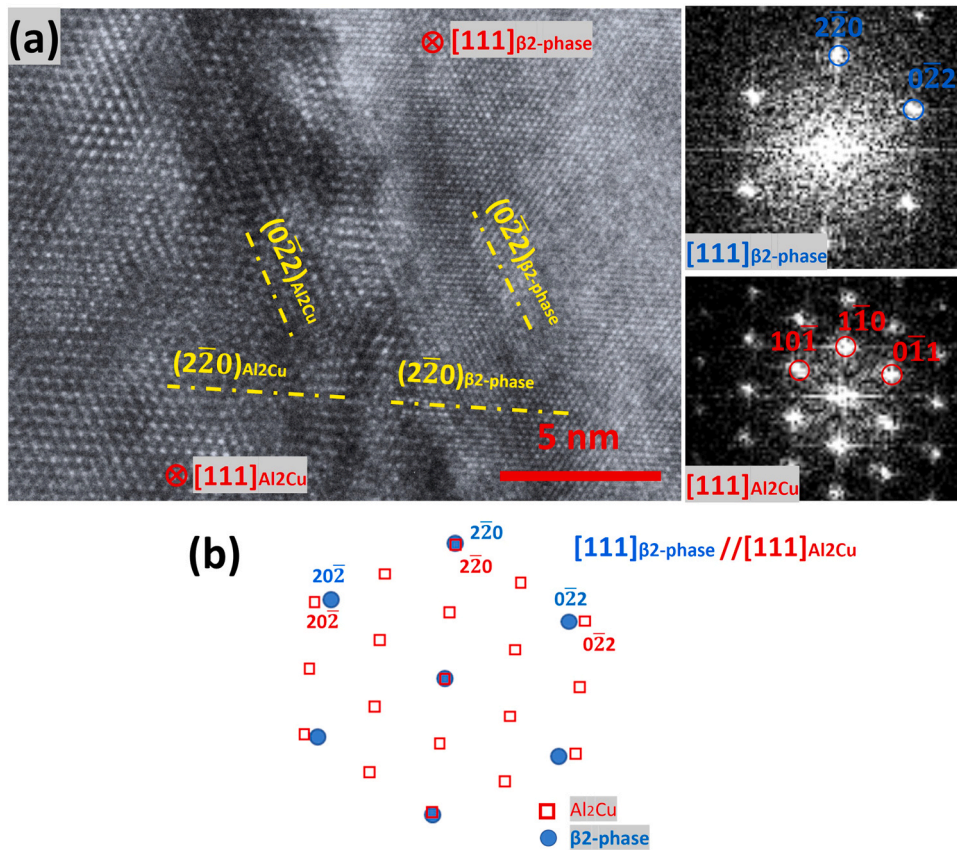

Fig. 11. (a) HRTEM image with FFT images showing the orientation relationship in Alloy B after annealing for 5 h at 500 °C (b) the schematic of the FFT diffraction pattern indexed along [1 1 1] axis for both the β_2 phase and Al$_2$Cu phase.
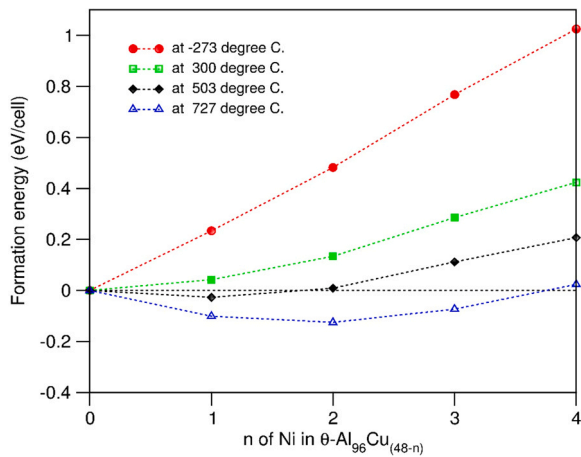
Fig. 12. Free energies of Ni solution at the Cu sites in θ-Al2Cu at −273.15 °C, 300 °C, 503 °C and 727 °C.

maximising the speed of growth (promoted by a small spacing). The absence of a Ni-containing phase favours rapid eutectic growth by minimising the interfacial energy and simplifying the diffusion path.

The first-principles calculations revealed that the solution of Ni at the Al sites in θ-Al$_2$Cu costs high energies (> 1.8 eV/Ni). Thus, it is unlikely for Ni substitution at the Al sites. The calculated formation energies for Ni solution at the Cu sites in θ-Al$_2$Cu according to Eq. (2)

at ambient conditions are plotted in Fig. 12. The calculations revealed moderate formation energies for Ni at the Cu sites in the crystal. The calculated formation energies are positive and increase almost linearly on the Ni content at ambient conditions. This means that Ni-containing θ-Al$_2$Cu is unfavourable at low temperatures. Solutions of Ni in the θ-Al$_2$Cu provide extra freedom in the system. This causes configurational entropy contributions to the free energy of the system at elevated temperature (T), $\Delta G(T) = \Delta H - T \Delta S_{conf}$. Here, ΔH is the change of enthalpy which is equal to the formation energy of the crystal at −273.15 °C when the zero-vibration contribution is ignored, $\Delta S_{conf} = \ln(w)$, where w is the number of configurations, is the configurational entropy. Using the random model, we calculated the free energies of the Ni -containing θ-Al$_2$Cu at elevated temperatures.

At low temperatures (< 300 °C), the calculations show that Ni-containing θ-Al$_2$Cu is unfavourable even with the configurational entropy contributions shown in Fig. 12. With the increase in temperature, the configurational entropy contribution becomes dominant. At 500 °C, about 1.4 at% Ni can be dissolved in this phase and at 730 °C, about 2.6 at% Ni can replace Cu in the structure. The calculations also revealed the reduction of the lattice parameter (volume) of the unit cell with Ni content, corresponding to the results obtained from SADPs in Fig. 5(a). This is due to the smaller volume of Ni as compared to that of Cu [63].

The hardness of the eutectic alloys is mainly affected by the type and size of the strengthening phases. From the hardness in Table 1, it can be found that the higher area fractions of a fine ternary eutectic
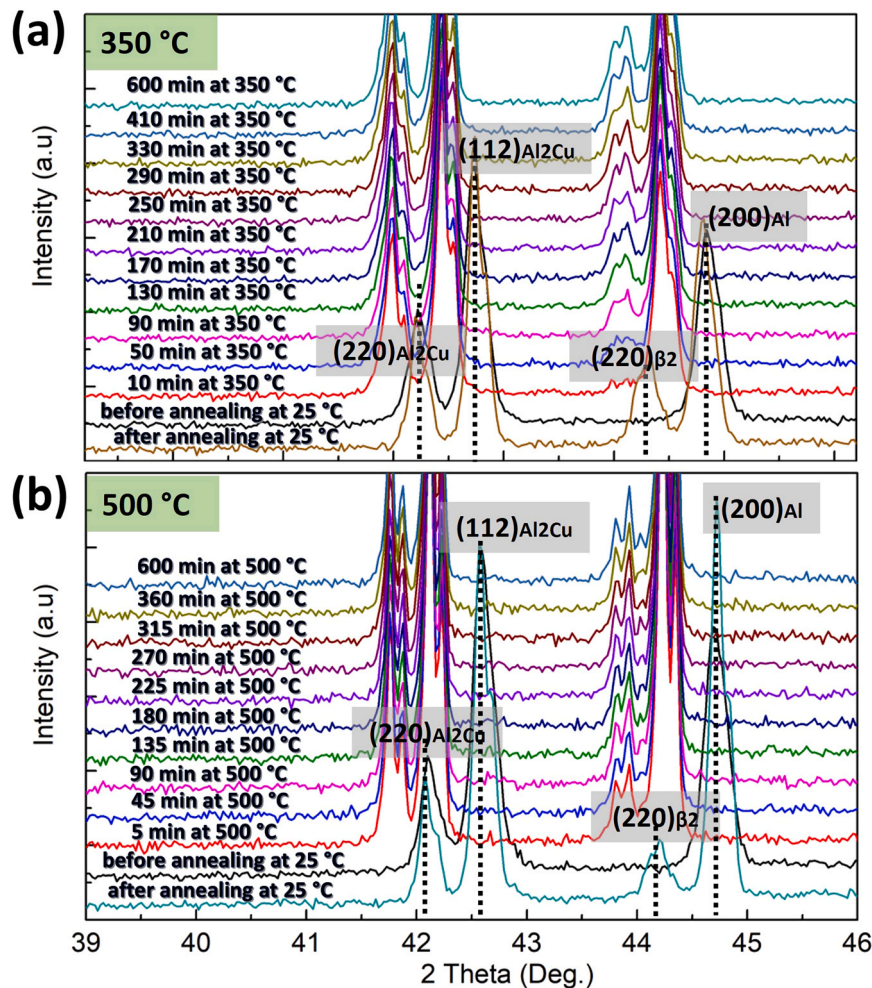

Fig. 13. In situ XRD spectrum with 2 Theta angle between 39° and 46° of Alloy B during annealing for different times as well as before and after annealing measured at 25 °C (a) annealing at 350 °C (b) annealing at 500 °C.
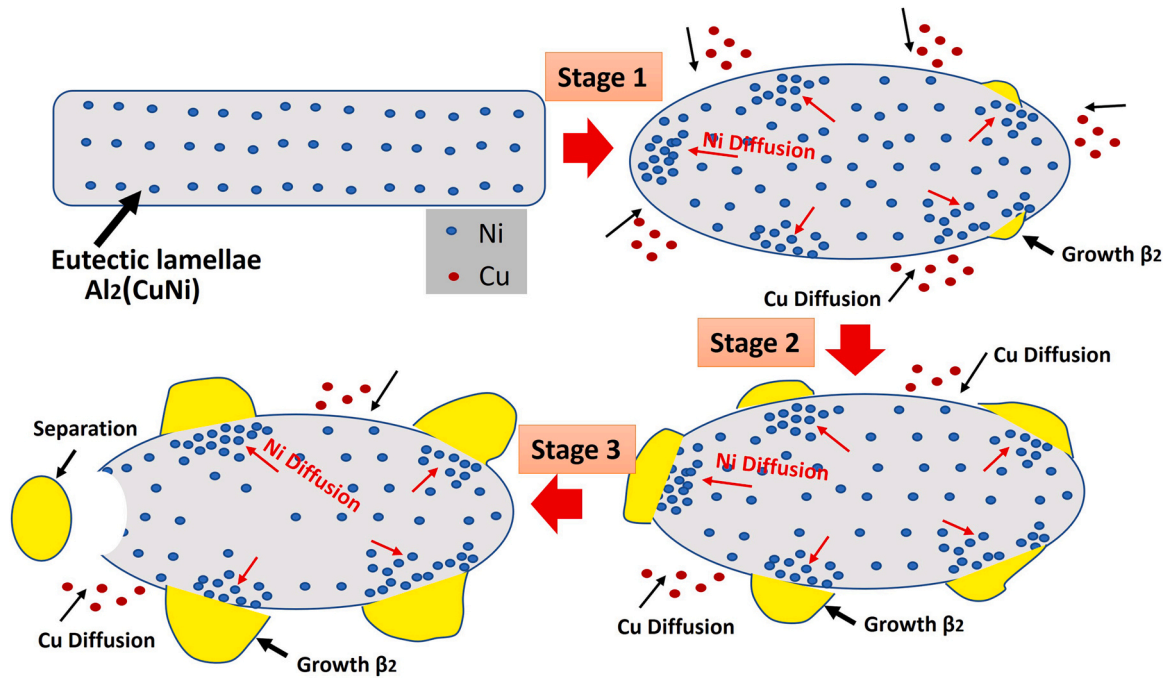
Fig. 14. The schematic illustration of phase transformation during annealing.

matrix in Al-Cu-Si-Ni alloys lead to higher hardness, and the ternary eutectic Al-Cu-Si-Ni alloy (Alloy B) has the highest hardness than other Al-Cu-Si-Ni alloys. The relationship between the size of the reinforcement phase and strength can be described by the Hall-Petch equation [64,65], which can be written as $\sigma_y = \sigma_e + K\lambda^{1/2}$. The σ_y is the yield strength, σ_e is friction strength, and λ is the interlamellar spacing. The ternary eutectic structure (α-Al+θ-Al$_2$(CuNi)+Si) has a finer interlamellar spacing than that in binary cellular eutectic structure, thus the eutectic Al-Cu-Si-Ni alloy has the highest hardness. In addition, the binary Al-Cu eutectic alloy has a similar hardness to that of the eutectic Al-Cu-Si-Ni alloy. But, the volume fraction of Al$_2$Cu phase in binary Al-33 wt%Cu alloy is higher than Al-24 wt%Cu-8 wt%Si-0.8 wt%Ni alloy according to their alloy compositions. There are three reasons. Firstly, the Al$_2$Cu phase in eutectic Al-Cu-Si-Ni alloy shows fragment and sphere morphology. It can provide more substrates between α-Al and Al$_2$Cu for dislocation pile up and the stress distribution are more uniform, compared with lamellar type morphology in binary Al-Cu eutectic alloy [54]. Secondly, the doping of Ni into Al$_2$Cu was studied by Zhou et al. [66]. It was found that the doping of Ni in Al$_2$Cu is able to increase interatomic interactions and the chemical bonds in the Al$_2$Cu crystals. Thus, the hardness of Al$_2$Cu can be improved by the dissolution of Ni into the structure. Consequently, the hardness of the alloy was increased. Lastly, the nanoscale fibrous Si phase can also make a contribution to the hardness of the alloy.

5.2. Thermal stability and phase transformation of ternary Al-Cu-Si-Ni eutectic alloy

The phase transformation was further confirmed by in situ XRD. Fig. 13 shows a series of XRD spectrum of Alloy B during annealing at 350 °C and 500 °C for different times as well as before and after annealing measured at 25 °C. The peaks with its corresponding plans and phases were labelled. All peaks shift to a smaller 2-Theta angle at high temperatures, due to the thermal expansion. The peak positions of the β_2 phase during and after annealing at 350 °C and 500 °C are both between 43.5° and 44.5°, respectively. This is the only peak which can be found in the XRD spectrum after and during

annealing. The peak position of the β_2 phase corresponds to the {220} plans which were identified from the XRD spectrum of FCC β_1-(Cu$_{2.9}$Ni$_{0.1}$)Al phase [47]. The phase transformation is accompanied by the development of peaks from β_2 phase with the annealing time in the XRD spectrum. In Fig. 13 (a), the formed peak is splitting at 350 °C at different times and the intensity of the formed peak increases with the time of annealing. The peak of the β_2 phase appears at 5 mins at 500 °C, and the splitting is more severe. The peak positions of β_2 phase are very close at 350 °C and 500 °C, indicating the very close crystal structure and lattice parameters. The reason for peak splitting in β_2 phase is the weakening of symmetry during phase transformation at high temperatures. It is known that at high temperatures, the process of phase transformation accompanied by atomic diffusion leads to some distortion in the FCC β_2 phase. Here, the {220} planes lose their symmetry and split into two peaks, corresponding to the crystal distortion from cubic to tetragonal. Moreover, the peak splitting at 350 °C and 500 °C is also found in peaks of $(220)_{Al2Cu}$ and $(112)_{Al2Cu}$. In Fig. 8(a), it can be found that the non-uniform distribution of the bright phase around the Al$_2$Cu phase occurred, which may result from the non-uniform distribution of Ni in the Al$_2$Cu particle before or during annealing at 350 °C. In addition, as shown in Fig. 12, the favourable Ni content in Al$_2$Cu is about 1.4 at% at about 500 °C. Therefore, there are Ni-rich and Ni-poor regions in Al$_2$Cu crystals. As mentioned before, the addition of Ni into the Al$_2$Cu crystal reduces its lattice parameters. As a result, the peak splitting of Al$_2$Cu phase is observed in samples prepared at 500 °C. In addition, the peak splitting of $(002)_{Al}$ might result from a solid solution of Cu and Si at high temperatures, and the distortion of α-Al is from cubic to tetragonal.

During annealing, the β_2 peak forms after annealing at 500 °C for 5 min, indicating the fast phase transformation at 500 °C. After annealing for 90 min at 350 °C, there is a distinct peak of β_2 phase. This indicates a much slower phase transformation at 350 °C and the microstructure stability of the alloy is related to the phase transformation including diffusion and growth β_2 phase. It is known that after the heat treatment in binary Al-Cu alloys, the fine eutectic Al$_2$Cu lamellae become coarse and spheroidised morphology which is driven by minimising the total area of the eutectic interfaces.

Simultaneously, this coarsening process is accompanied by the necking and dissolution of the Al_2Cu phase [67], due to the high solubility and diffusion coefficient of Cu in α-Al. The coarsening of Al_2Cu is detrimental to the mechanical properties of Al-Cu based alloys. Interestingly, the Al_2Cu phase shows finer microstructure in Alloy B than that in Alloy A after annealing. The microstructure evolution in Alloy B during annealing has three stages based on experimental observations, and the schematic illustration is shown in Fig. 14. In the first stage, the Al_2Cu phase with the dissolution of Ni is at non-equilibrium state processed under rapid solidification in suction casting, and the diffusion of Ni inside the Al_2Cu phase occurs after annealing at high temperatures. Also, Ni has very low solubility in α-Al and its diffusion into α-Al is very limited, while Cu can diffuse into α-Al. The Ni diffuses towards the edge of the Al_2Cu phase, forming a composition gradient. Meanwhile, Cu diffuses towards the adjacent Al_2Cu phase through α-Al, feeding the growth of the Al_2Cu phase. Some small β_2 phases nucleated and grow at the edge of the Al_2Cu phase. The composition gradient and small β_2 phases are able to provide the barriers to the diffusion of Cu, resulting in the slow growth of the Al_2Cu phase. In stage 2, the Ni further diffuses into the edge, and more β_2 phases form. Further growth of existing β_2 takes place. At the same time, the β_2 phase can act as a barrier for the growth of the Al_2Cu phase. In another word, the free growth of the Al_2Cu phase is restricted by β_2 phase. In the last stage, the Al_2Cu phase is spheroidised and coarsened, and some β_2 phase is detached. It corresponds to the microstructure in Fig. 8(c) and (d), which shows the dual-size distribution of the intermetallic phase. The internal Ni diffusion in the third stage is less compared with the beginning, as indicated by the Ni content of Al_2Cu in Table 2. It is because there is a limited amount of Ni in Al_2Cu phase providing the growth of β_2 phase at this stage. Thus, the composition of Ni in β_2 phases tends to be stable at this stage.

The annealing temperature plays a dominating role in the speed of the phase transformation process. At 350 °C for 168 h, a bright layer and small β_2 phases were found in the microstructure as shown in Fig. 8(a). Also, the formation of the β_2 phase has a lower Ni content, as shown in Table 2. These indicate the microstructure evolution is still in the first stage. The finer microstructure in Alloy B compared with Alloy A after annealing at this temperature is because of the composition gradient and small β_2 phases in Al_2Cu phases. However, at 500 °C for 9 h, there are a few β_2 phases detached and attached to the Al_2Cu phase, as shown in Fig. 8(c). It corresponds to Stage 3 in Fig. 14. The finer microstructure in Alloy B compared with Alloy A after annealing at 500 °C is because of the composition gradient and small β_2 phase adjacent to Al_2Cu phase in the first stage as well as the growth restriction of β_2 phase in a later stage. Lastly, the size of β_2 phase in Alloy B changes very slightly after exposure at 500 °C for different times, which indicates its high thermal stability. It is reported that high entropy B2 aluminides with the same lattice containing multiple transition elements such as $(Fe_{1/4}Co_{1/4}Ni_{1/4}Cr_{1/4})Al$, $(Fe_{1/4}Co_{1/4}Ni_{1/4}Cu_{1/4})Al$ and $(Fe_{1/5}Co_{1/5}Ni_{1/5}Mn_{1/5}Cu_{1/5})Al$ have high thermal stability at elevated temperature, due to their high configurational entropy [68]. Here, the FCC β_2 phase has a fixed crystal structure and a constant lattice parameter during phase transformation, but various content of Ni depending on the temperature. The dissolution of Ni in this FCC crystal structure is able to enhance the high configuration entropy, leading to a decrease of Gibbs free energy. Thus, high thermal stability can be achieved.

6. Conclusions

1. The ternary $Al/Si/\theta$-$Al_2(CuNi)$ eutectic in the quaternary Al-Cu-Si-Ni system was shown to have a eutectic composition of Al67.2Cu24Si8Ni0.8 (wt%) and a eutectic temperature of 523 °C. The ternary eutectic alloy was then prepared by arc melting and suction casting.

2. The hardness of the ternary $Al/Si/\theta$-$Al_2(CuNi)$ eutectic is higher than some other off-eutectic Al-Cu-Si-Ni alloys but is very close to that of the binary Al/θ-Al_2Cu eutectic.

3. The eutectic solidification is accompanied by cooperative growth of α-Al, Si and Al_2Cu phases. The Al_2Cu phase shows fragmented lamellar morphology with a lamellar thickness of 130 ± 30 nm, and Si has fibrous morphology with a size below 100 nm.

4. The dissolution of Ni (1.7 at%) in Al_2Cu phase was found in the eutectic alloy after rapid solidification. First-principles DFT calculations revealed that configurational entropy contributed to the stabilised Ni-containing Al_2Cu phase at high temperatures.

5. Phase transformation occurs after post-solidification annealing. β_2 phase $(Al_3(CuNi)_2)$ was found after annealing both at 350 °C and 500 °C, which has $\beta1$-$(Cu_{2.9}Ni_{0.1})$-type crystal structure.

6. This microstructure of ternary eutectic alloy has better thermal stability than binary Al/θ-Al_2Cu eutectic, and there is potential for its use at elevated temperatures up to 350 °C.

CRediT authorship contribution statement

Qing Cai: Conceptualization, Methodology, Investigation, Writing – original draft, Writing – review & editing. **Changming Fang**: Conceptualization, Calculation, Writing – review & editing. **Chamini L. Mendis:** Methodology, Investigation, Writing – review & editing. **Isaac T.H Chang:** Conceptualization, Writing – review & editing, Supervision. **Brian Cantor:** Conceptualization, Writing – review & editing, Methodology, Investigation.

Data Availability

The authors do not have permission to share data.

Declaration of Competing Interest

The authors declare that they have no known competing financial interests or personal relationships that could have appeared to influence the work reported in this paper.

Acknowledgements

Appendix A. Supporting information

Supplementary data associated with this article can be found in the online version at doi:10.1016/j.jallcom.2023.168942.

References

[1] E. Georgantzia, M. Gkantou, G.S. Kamaris, Aluminium alloys as structural material: a review of research, Eng. Struct. 227 (2021) 111372, https://doi.org/10.1016/j.engstruct.2020.111372

[2] R.A. Michi, A. Plotkowski, A. Shyam, R.R. Dehoff, S.S. Babu, Towards high-temperature applications of aluminium alloys enabled by additive manufacturing, Int. Mater. Rev. 67 (2022) 298–345, https://doi.org/10.1080/09506608.2021.1951580

[3] A. Shyam, S. Bahl, Heat-resistant aluminium alloys, Nat. Mater. (2022) 1–2, https://doi.org/10.1038/s41563-022-01436-6

[4] C.S. Tiwary, P. Pandey, S. Sarkar, R. Das, S. Samal, K. Biswas, K. Chattopadhyay, Five decades of research on the development of eutectic as engineering materials, Prog. Mater. Sci. 123 (2022) 100793, https://doi.org/10.1016/j.pmatsci.2021.100793

[5] Y. Zhang, R. Li, P. Chen, X. Li, Z. Liu, Microstructural evolution of Al2Cu phase and mechanical properties of the large-scale Al alloy components under different consecutive manufacturing processes, J. Alloy. Compd. 808 (2019) 151634, https://doi.org/10.1016/j.jallcom.2019.07.346

[6] J. Zhang, B. Wang, Y. Tian, Study of pre-strain before artificial aging on mechanical property and stress corrosion behavior of 2297 Al–Cu–Li alloy, Mater. Sci. Eng. A. 831 (2022) 142174, https://doi.org/10.1016/j.msea.2021.142174

[7] S. Bahl, L. Xiong, L.F. Allard, R.A. Michi, J.D. Poplawsky, A.C. Chuang, D. Singh, T.R. Watkins, D. Shin, J.A. Haynes, A. Shyam, Aging behavior and strengthening mechanisms of coarsening resistant metastable θ' precipitates in an Al–Cu alloy, Mater. Des. 198 (2021) 109378, https://doi.org/10.1016/j.matdes.2020.109378

[8] B. Milligan, D. Ma, L. Allard, A. Clarke, A. Shyam, Crystallographic orientation-dependent strain hardening in a precipitation-strengthened Al-Cu alloy, Acta Mater. 205 (2021) 116577, https://doi.org/10.1016/j.actamat.2020.116577

[9] B. Cantor, G.A. Chadwick, The tensile deformation of unidirectionally solidified Al-Al3Ni and Al-Al2Cu eutectics, J. Mater. Sci. 10 (1975) 578–588, https://doi.org/10.1007/BF00566564

[10] B. Cantor, G.J. May, G.A. Chadwick, The tensile fracture behaviour of the aligned Al-Al3Ni and Al-CuAl2 eutectics at various temperatures, J. Mater. Sci. 8 (1973) 830–838, https://doi.org/10.1007/BF02397911

[11] Q. Lei, J. Wang, A. Misra, Mechanical behavior of al–al2 cu–si and al–al2 cu eutectic alloys, Crystals 11 (2021) 1–9, https://doi.org/10.3390/cryst11020194

[12] S.J.J. Wang, D.Y.Y. Xie, J. Wang, A. Misra, Deformation behavior of nanoscale Al–Al2Cu eutectics studied by in situ micropillar compression, Mater. Sci. Eng. A. 800 (2021) 140311, https://doi.org/10.1016/j.msea.2020.140311

[13] B.J. Kim, A.K. Dahle, Y.H. Park, Y.C. Lee, The effect of Sr additions on Al–Cu–Si ternary eutectic alloys for a high-ductility bimodal microstructure, Mater. Sci. Eng. A. 833 (2022) 142547, https://doi.org/10.1016/j.msea.2021.142547

[14] Q. Lei, J. Wang, A. Misra, Mechanical Behavior of Al–Al2Cu–Si and Al–Al2Cu eutectic alloys, Crystals 11 (2021) 194, https://doi.org/10.3390/cryst11020194

[15] J.M. Park, K.B. Kim, D.H. Kim, N. Mattern, R. Li, G. Liu, J. Eckert, Multi-phase Al-based ultrafine composite with multi-scale microstructure, Intermetallics 18 (2010) 1829–1833, https://doi.org/10.1016/j.intermet.2010.02.042

[16] C.S. Tiwary, S. Kashyap, K. Chattopadhyay, Development of alloys with high strength at elevated temperatures by tuning the bimodal microstructure in the Al-Cu-Ni eutectic system, Scr. Mater. 93 (2014) 20–23, https://doi.org/10.1016/j.scriptamat.2014.08.020

[17] D. Ezemenaka, A. Genau, Crystal orientation relationships and pattern evolution in directionally solidified Al-Cu-Mg ternary eutectic, J. Cryst. Growth 577 (2022) 126389, https://doi.org/10.1016/j.jcrysgro.2021.126389

[18] D. Ezemenaka, C. Patino, A. Genau, Microstructural evolution in directionally solidified Al-Cu-Mg ternary eutectic, J. Alloy. Compd. 883 (2021) 160818, https://doi.org/10.1016/j.jallcom.2021.160818

[19] E. Çadirli, H. Kaya, D. Räbiger, S. Eckert, M. Gündüz, Effect of rotating magnetic field on the microstructures and physical properties of Al-Cu-Co ternary eutectic alloy, J. Alloy. Compd. 647 (2015) 471–480, https://doi.org/10.1016/j.jallcom.2015.05.162

[20] Q. Cai, B. Cantor, V.S. Tong, F. Wang, C.L. Mendis, I.T.H. Chang, Z. Fan, Microstructure and mechanical properties of ultrafine quaternary al-cu-si-mg eutectic alloy, Met. (Basel) 12 (2022) 7, https://doi.org/10.3390/met12010007

[21] U. Büyük, S. Engin, H. Kaya, E. Çadırlı, N. Maraşlı, Directionally solidified Al–Cu–Si–Fe quaternary eutectic alloys, Phys. Met. Metallogr. 121 (2020) 78–83, https://doi.org/10.1134/S0031918×20010044

[22] J. Tang, C. Liang, C. Xu, Effects of alloying elements and temperature on thermodynamic state and microstructure of piston aluminum alloy, Defect Diffus. Forum 417 (2022) 3–8, https://doi.org/10.4028/p-1421c8

[23] F. Czerwinski, M. Aniolek, J. Li, Strengthening retention and structural stability of the Al-Al3Ni eutectic at high temperatures, Scr. Mater. 214 (2022) 114679, https://doi.org/10.1016/j.scriptamat.2022.114679

[24] F. Czerwinski, Thermal stability of aluminum-nickel binary alloys containing the Al-Al3Ni eutectic, Metall. Mater. Trans. A. 52 (2021) 4342–4356, https://doi.org/10.1007/s11661-021-06372-9

[25] L. Zuo, B. Ye, J. Feng, H. Zhang, X. Kong, H. Jiang, Effect of ε-Al3Ni phase on mechanical properties of Al–Si–Cu–Mg–Ni alloys at elevated temperature, Mater. Sci. Eng. A. 772 (2020) 138794, https://doi.org/10.1016/j.msea.2019.138794

[26] S.A. Awe, S. Seifeddine, A.E.W. Jarfors, Y.C. Lee, A.K. Dahle, Development of new Al-Cu-Si alloys for high temperature performance, Adv. Mater. Lett. 8 (2017) 695–701, https://doi.org/10.5185/amlett.2017.1471

[27] F. Czerwinski, Thermal stability of aluminum-nickel binary alloys containing the Al-Al3Ni eutectic, Metall. Mater. Trans. A. 52 (2021) 4342–4356, https://doi.org/10.1007/s11661-021-06372-9

[28] Y. Guo, J. Hu, Q. Han, B. Sun, J. Wang, C. Liu, Microstructure diversity dominated by the interplay between primary intermetallics and eutectics for Al-Ce heat-resistant alloys, J. Alloy. Compd. 899 (2022) 162914, https://doi.org/10.1016/j.jallcom.2021.162914

[29] F. Czerwinski, Thermal stability of aluminum–cerium binary alloys containing the Al-Al11Ce3 eutectic, Mater. Sci. Eng. A. 809 (2021) 140973, https://doi.org/10.1016/j.msea.2021.140973

[30] W. Wang, N. Takata, A. Suzuki, M. Kobashi, M. Kato, High-temperature strength sustained by nano-sized eutectic structure of Al–Fe alloy manufactured by laser powder bed fusion, Mater. Sci. Eng. A. 838 (2022) 142782, https://doi.org/10.1016/j.msea.2022.142782

[31] W. Yu, Q. Hao, L. Fan, J. Li, Eutectic solidification microstructure of an Al-4Ni-2Mn alloy, J. Alloy. Compd. 688 (2016) 798–803, https://doi.org/10.1016/j.jallcom.2016.07.259

[32] S. Bahl, L. Xiong, L.F. Allard, R.A. Michi, J.D. Poplawsky, A.C. Chuang, D. Singh, T.R. Watkins, D. Shin, J.A. Haynes, A. Shyam, Aging behavior and strengthening mechanisms of coarsening resistant metastable θ' precipitates in an Al–Cu alloy, Mater. Des. 198 (2021) 109378, https://doi.org/10.1016/j.matdes.2020.109378

[33] B. Milligan, D. Ma, L. Allard, A. Clarke, A. Shyam, Dislocation-θ' (Al2Cu) interactions during creep deformation of an Al-Cu alloy, Scr. Mater. 217 (2022) 114739, https://doi.org/10.1016/j.scriptamat.2022.114739

[34] J.U. Rakhmonov, S. Bahl, A. Shyam, D.C. Dunand, Cavitation-resistant intergranular precipitates enhance creep performance of θ'-strengthened Al-Cu based alloys, Acta Mater. 228 (2022) 117788, https://doi.org/10.1016/j.actamat.2022.117788

[35] T. Wu, A. Plotkowski, A. Shyam, D.C. Dunand, Microstructure and creep properties of cast near-eutectic Al-Ce-Ni alloys, Mater. Sci. Eng. A. 833 (2022) 142551, https://doi.org/10.1016/j.msea.2021.142551

[36] D. Wang, H. Ning, B. Wang, G. Liu, S. Yuan, Fabrication of a NiAl–Cr(Mo) eutectic alloy with network microstructure for high-temperature strengthening, Mater. Sci. Eng. A. 835 (2022) 142628, https://doi.org/10.1016/j.msea.2022.142628

[37] A. Meetsma, J.L. De Boer, S. Van Smaalen, Refinement of the crystal structure of tetragonal Al2Cu, J. Solid State Chem. 83 (1989) 370–372, https://doi.org/10.1016/0022-4596(89)90188-6

[38] N.A. Belov, D.G. Eskin, N.N. Avxentieva, Constituent phase diagrams of the Al-Cu-Fe-Mg-Ni-Si system and their application to the analysis of aluminium piston alloys, Acta Mater. 53 (2005) 4709–4722, https://doi.org/10.1016/j.actamat.2005.07.003

[39] G. Kresse, J. Furthmüller, Efficiency of ab-initio total energy calculations for metals and semiconductors using a plane-wave basis set, Comput. Mater. Sci. 6 (1996) 15–50, https://doi.org/10.1016/0927-0256(96)00008-0

[40] P.E. Blöchl, Projector augmented-wave method, Phys. Rev. B. 50 (1994) 17953–17979, https://doi.org/10.1103/PhysRevB.50.17953

[41] J.P. Perdew, K. Burke, M. Ernzerhof, Generalized gradient approximation made simple, Phys. Rev. Lett. 77 (1996) 3865–3868, https://doi.org/10.1103/PhysRevLett.77.3865

[42] J. Hubbard, Electron correlations in narrow energy bands, Proc. R. Soc. Lond. Ser. A. Math. Phys. Sci. 276 (1963) 238–257, https://doi.org/10.1098/rspa.1963.0204

[43] M. Souissi, C.M. Fang, R. Sahara, Z. Fan, Formation energies of θ-Al2Cu phase and precursor Al-Cu compounds: importance of on-site Coulomb repulsion, Comput. Mater. Sci. 194 (2021), https://doi.org/10.1016/j.commatsci.2021.110461

[44] L. Wang, T. Maxisch, G. Ceder, Oxidation energies of transition metal oxides within the GGA+U framework, Phys. Rev. B Condens. Matter Mater. Phys. 73 (2006) 195107, https://doi.org/10.1103/PhysRevB.73.195107

[45] H.J. Monkhorst, J.D. Pack, Special points for Brillouin-zone integrations, Phys. Rev. B. 13 (1976) 5188–5192, https://doi.org/10.1103/PhysRevB.13.5188

[46] K.A. Jackson, J.D. Hunt, Lamellar and Rod Eutectic Growth, Dyn. Curved Front, Elsevier, 1988, pp. 363–376, https://doi.org/10.1016/B978-0-08-092523-3.50040-X

[47] M.J. Duggin, Further studies of martensitic transformations in gold-copper-zinc and copper-aluminium-nickel alloys, Acta Met. 14 (1966) 123–129, https://doi.org/10.1016/0001-6160(66)90293-8

[48] M. Warmuzek, Chemical composition of the Ni-containing intermetallic phases in the multicomponent Al alloys, J. Alloy. Compd. 604 (2014) 245–252, https://doi.org/10.1016/j.jallcom.2014.03.119

[49] F.R.N. Frank, R.N. Nabarro, M.S. Duesbery, J.P. Hirth, Dislocations in Solids, North-Holland Pub, Co, 1979.

[50] L. Mondolfo, Aluminum alloys: structure and properties, 1976. ⟨https://books.google.com/books?hl=en&lr=&id=Xf4kBQAAQBAJ&oi=fnd&pg=PP1&ots=Q53C1mJusd&sig=TidoDSJe5iRLCNZRLSjHxO53ZUU⟩ (accessed September 29, 2019).

[51] T.P. Yadav, N.K. Mukhopadhyay, R.S. Tiwari, O.N. Srivastava, Formation of Al3Ni2-type nanocrystalline 3 phases in the Al-Cu-Ni system by mechanical alloying, Philos. Mag. Lett. 87 (2007) 781–789, https://doi.org/10.1080/09500830701573350

[52] L.A. Matlakhova, E.C. Pereira, S.A. Pulnev, C.Y. Shigue, N.A. Palii, Physical and structural characterization of monocrystalline Cu-13.7% Al-4.2% Ni alloy submitted to thermo-cyclical treatments under applied loads, Met. (Basel) 10 (2020) 219, https://doi.org/10.3390/met10020219

[53] I. Shishkovsky, I. Yadroitsev, Y. Morozov, Laser-assisted synthesis in Cu-Al-Ni system and some of its properties, J. Alloy. Compd. 658 (2016) 875–879, https://doi.org/10.1016/j.jallcom.2015.10.299

[54] B.J. Kim, A.K. Dahle, Y.H. Park, Y.C. Lee, The effect of Sr additions on Al–Cu–Si ternary eutectic alloys for a high-ductility bimodal microstructure, Mater. Sci. Eng. A. 833 (2022) 142547, https://doi.org/10.1016/j.msea.2021.142547

[55] Q. Cai, C.L. Mendis, I.T.H. Chang, Z. Fan, Microstructure evolution and mechanical properties of new die-cast Al-Si-Mg-Mn alloys, Mater. Des. 187 (2020) 108394, https://doi.org/10.1016/j.matdes.2019.108394

[56] Y. Kaygisiz, N. Maraşli, Microstructural, mechanical and electrical characterization of directionally solidified Al-Si-Mg eutectic alloy, J. Alloy. Compd. 618 (2015) 197–203, https://doi.org/10.1016/j.jallcom.2014.08.056

[57] Ü. Bayram, N. Maraşlı, Influence of growth rate on eutectic spacing, micro-hardness, and ultimate tensile strength in the directionally solidified Al-Cu-Ni eutectic alloy, Metall. Mater. Trans. B Process. Metall. Mater. Process. Sci. 49 (2018) 3293–3305, https://doi.org/10.1007/s11663-018-1404-7

[58] J. De Wilde, L. Froyen, S. Rex, Coupled two-phase [α(Al) + θ(Al2Cu)] planar growth and destabilisation along the univariant eutectic reaction in Al-Cu-Ag alloys, Scr. Mater. 51 (2004) 533–538, https://doi.org/10.1016/j.scriptamat.2004.05.040

[59] W. Kurz, R. Trivedi, Eutectic growth under rapid solidification conditions, Metall. Trans. A. 22 (1991) 3051–3057, https://doi.org/10.1007/BF02650266

[60] R. Trivedi, P. Magnin, W. Kurz, Theory of eutectic growth under rapid solidification conditions, Acta Met. 35 (1987) 971–980, https://doi.org/10.1016/0001-6160(87)90176-3

[61] D. Ezemenaka, C. Patino, A. Genau, Microstructural evolution in directionally solidified Al-Cu-Mg ternary eutectic, J. Alloy. Compd. 883 (2021) 160818, https://doi.org/10.1016/j.jallcom.2021.160818

[62] U. Böyük, N. Maraşlı, H. Kaya, E. Çadırlı, K. Keşlioğlu, Directional solidification of Al-Cu-Ag alloy, Appl. Phys. A Mater. Sci. Process. 95 (2009) 923–932, https://doi.org/10.1007/s00339-009-5130-5

[63] J.W. Arblaster, Selected Values of the Crystallographic Properties of Elements, 2018. ⟨https://books.google.co.uk/books?hl=zh-CN&lr=&id=ITpsDwAAQBAJ&oi=fnd&pg=PR14&dq=Arblaster,+J.+W.+Selected+values+of+the+crystallographic+properties+of+the+elements,+ASM+In-ternational,+Materials+Park,+Ohio,+USA,+2018%3B+pp.+118–228.&ots=lC3Va1MFkR&sig=nBw⟩ (accessed May 30, 2022).

[64] E.O. Hall, The deformation and ageing of mild steel: III discussion of results, Proc. Phys. Soc. Sect. B. 64 (1951) 747–753, https://doi.org/10.1088/0370-1301/64/9/303

[65] N.J. Petch, The cleavage strength of polycrystals, J. Iron Steel Inst. 174 (1953) 25–28 ⟨https://ci.nii.ac.jp/naid/10019881123⟩ (accessed July 1, 2020).

[66] Z. Zhou, H. Bao, K. Zheng, B. Pan, H. Wang, The structures, stability, mechanical properties and electronic properties of X (X=Nb, Ge, Ni) doped Al2Cu: a first-principle study, Mater. Res. Express 6 (2019) 1165b5, https://doi.org/10.1088/2053-1591/ab4df0

[67] Y.M. Han, A.M. Samuel, F.H. Samuel, H.W. Doty, Dissolution of Al2Cu phase in non-modified and Sr modified 319 type alloys, Int. J. Cast. Met. Res. 21 (2008) 387–393, https://doi.org/10.1179/136404608×347662

[68] N. Zhou, S. Jiang, T. Huang, M. Qin, T. Hu, J. Luo, Single-phase high-entropy in-termetallic compounds (HEICs): bridging high-entropy alloys and ceramics, Sci. Bull. 64 (2019) 856–864, https://doi.org/10.1016/j.scib.2019.05.007